coatings

MDPI

Article

Droplet Dynamics and Freezing Delay on Nanoporous Microstructured Surfaces at Condensing Environment

Asif Raiyan, Behrouz Mohammadian and Hossein Sojoudi *

Department of Mechanical, Industrial and Manufacturing Engineering, The University of Toledo, Toledo, OH 43606, USA; asif.raiyan@rockets.utoledo.edu (A.R.); behrouz.mohammadian@rockets.utoledo.edu (B.M.)
* Correspondence: hossein.sojoudi@utoledo.edu

Abstract: Superhydrophobic surfaces have aroused great interest for being promising candidates in applications such as self-cleaning, anti-icing, and corrosion resistance. However, most of the superhydrophobic surfaces lose their anti-wettability in low surface temperature and high humidity. The loss of superhydrophobicity by condensed liquid is a very common practical incident, yet to be understood properly. Here we report the wettability of the superhydrophobic nanoporous surfaces in condensation and freezing environments. Various structured surfaces fabricated with carbon nanotubes (CNT) and coated by an ultrathin, conformal, and low surface energy layer of poly (1H,1H,2H,2H-perfluorodecylacrylate) (pPFDA) are exploited in humid conditions. Droplet impact dynamics, condensate characteristics, and freezing time delays are investigated on the CNT micropillars with various geometries along with the CNT forest and two commercially available anti-wetting coatings, NeverWet and WX2100. Nanoporous microstructured CNT pillars with the favorable topological configuration demonstrated complete droplet bouncing, significant freezing delays, and considerable durability during several icing/de-icing cycles. This study provides an understanding on the preferable geometry of the highly porous CNT micropillars for retaining hydrophobicity and preventing ice formation, which is of practical importance for the rational development of anti-wetting surfaces and their applications in low temperatures and humid conditions.

Keywords: condensate coalescence; Cassie-Baxter; anti-icing; nanoporous microstructures; freezing delay; droplet dynamics

check for updates

Citation: Raiyan, A.; Mohammadian, B.; Sojoudi, H. Droplet Dynamics and Freezing Delay on Nanoporous Microstructured Surfaces at Condensing Environment. *Coatings* **2021**, *11*, 617. https://doi.org/10.3390/coatings11060617

Academic Editor: Artur P. Terzyk

Received: 4 May 2021
Accepted: 18 May 2021
Published: 21 May 2021

Publisher's Note: MDPI stays neutral with regard to jurisdictional claims in published maps and institutional affiliations.

Copyright: © 2021 by the authors. Licensee MDPI, Basel, Switzerland. This article is an open access article distributed under the terms and conditions of the Creative Commons Attribution (CC BY) license (https://creativecommons.org/licenses/by/4.0/).

1. Introduction

Droplet repellency on anti-wetting solid surfaces has been an active research field in the past two decades [1–5]. Studying liquid interaction with the anti-wetting surfaces is of great importance for numerous technical and industrial applications such as self-cleaning, anti-fogging, anti-icing, anti-fouling, and dropwise condensation, among others [6–12]. Superhydrophobic surfaces have shown excellent anti-wetting properties identified by high water contact angle (WCA) and very small WCA hysteresis (difference between advancing and receding WCA) [13]. Some of these surfaces typically have very low surface energy with micro-scale, nano-scale, and/or hierarchical features that enable entrapping a thin air layer between them and the droplet [14–17]. More recently, superhydrophobic surfaces have also shown some promise in delay of icing with potential applications in power lines, wind turbines, photovoltaic panels, and other infrastructures [18–23]. Some other anti-icing performances exhibited by the superhydrophobic surfaces include lowering ice adhesion strength, repelling freezing rain droplets, and delaying frost formation [13,24–30]. However, under harsh environmental conditions like low temperatures and high humidity, these surfaces lose their superhydrophobicity and fail to exhibit those anti-icing features [31–34]. When humid air encounters a surface that is colder than the air and cools to its dew point, condensate water droplets nucleate on the surface and grow by time [35,36]. Condensation on solid surfaces is a common scenario in nature, which has always been a threat to the

immense applications of the superhydrophobic surfaces for icing mitigation [37,38]. Condensate droplets infiltrate the roughness/features of the surfaces, wetting them [39]. Therefore, most of the superhydrophobic surfaces lose their water repelling and anti-icing features in low temperature and high humidity conditions, due to nucleation and growth of the condensate droplets. This sometimes leads to potential enhanced formation of frost depending on the temperature [30,40,41]. The subsequent freezing of the condensate droplets mechanically anchors them to surface roughness and leads to enhanced ice/frost build up on them, with increased adhesion strength [42,43]. It has been shown that the anti-icing performance of the superhydrophobic surfaces deteriorates after several icing/de-icing cycles [37,44]. Moreover, damages on surface textures have been shown during icing and de-icing, due to the expansion induced by melting ice [37,39,45,46]. Initially, Lafuma et al. demonstrated that the WCA hysteresis increased to 100° when the condensate droplets were grown on a superhydrophobic surface, compared to only 5° on the same dry surface [47,48]. Moreover, advancing WCA was observed to be 141° in condensation condition (high humidity and low temperature), instead of 164° in the dry condition. Understanding wettability and mechanisms of wetting transition are explicitly discussed on nanoporous surfaces [49,50]. Wang et al. discussed the non-equilibrium condensed droplet morphologies by local energy barriers and nucleation-mediated droplet–droplet interactions, which leads to Wenzel state [42]. Narhe et al. showed results of condensation on strip and square patterned superhydrophobic surfaces to understand the condensate droplet evolution [51]. Rykaczewski et al. showed the mechanism of condensate microdroplet growth on nanostructured superhydrophobic surfaces both experimentally and theoretically by a quantitative model [52]. Later by the same group, application of hygroscopic drops was demonstrated for inhibiting condensation based frost formation between microscopic and macroscopic arrays of propylene glycol and salt saturated water drops [53,54]. Varanasi et al. showed rare-earth oxide ceramics materials promoted dropwise condensation, repelling water droplets and sustaining hydrophobicity even after exposure to harsh environments [55]. Other ceramic membranes grafted and coated by perfluorosilane showed promising results [56–59]. In condensate condition, self-cleaning of superhydrophobic surfaces by self-propelled droplet jumping and sweeping have also been demonstrated by several studies [30,32,60–62]. Oberli et al. studied condensation of water onto physically-decorated substrates and its associated impact on the freezing of macroscopic droplets on them [39]. The formation of drops that are partly in the Cassie and partly in the Wenzel mode has also been observed on a post surface [34,63]. Certain artificially-prepared nanostructured materials exhibited condensate drops in Cassie state. Dorrer et al. mentioned that if the roughness features are on the same size scale as the smallest condensate drops, the surface might maintain Cassie state for a while [35,64]. Recently, Lambley et al. discussed a trend of increasing impalement severity with decreasing ambient pressure and elucidated a condensation-based impalement mechanism within the texture resulting from the compression of intervening gas layer between the impacting droplet and the surface texture [65]. Condensation and frost growth were temporally controlled by passive suppression of inter-droplet frost growth with chemical micropattern design, leading to consequent control of freezing events [62]. These studies confirmed that a Wenzel wetting state was induced by the condensate droplets on the superhydrophobic surfaces. However, little consideration has been given to understand the effect of surface features on demonstrating delay in freezing that is preceded by condensation. In addition, droplet dynamics on pattered micro/nanostructure surfaces has not been well studied in condensation condition. Additionally, there has not been any study demonstrating formation of Cassie droplets due to coalesce of condensate droplets on micro/nano patterned surfaces.

Here, droplet dynamics and freezing delay in condensation condition is studied on nanoporous microstructured surfaces made of carbon nanotube (CNT) forest and CNT micropillars coated with poly (1H,1H,2H,2H-perfluorodecylacrylate) (pPFDA). The performances of these samples are compared with two commercially available superhydrophobic coatings (NeverWet, Rust-Oleum, Vernon Hills, IL, USA and WX2100, Cytonix, Beltsville,

MD, USA). We show that the nanoporous microstructured surfaces exhibit complete repelling of the incoming droplets even in condensation conditions. We also study the impact of micropillar geometry on freezing delay during direct freezing and condensation, followed by freezing conditions. We observe two opposite trends in freezing delays during these two different freezing conditions. We demonstrate that the coalescence behavior of the condensate droplets on the top of the micropillars and on the cavities can be controlled by modulating the geometry of the micropillars to form non-wetting Cassie droplets. Finally, we study the nanoporous microstructured surfaces through multiple icing/deicing cycles for assessing their durability. This study aims to develop robust surfaces that exhibit hydrophobic and icephobic natures even at high humidity and low temperature environmental conditions.

2. Materials and Methods

2.1. Synthesis of Nanoporous Microstructured Surfaces

The synthesis of CNT forest and CNT micropillars, along with the iCVD polymerization, was described in details in our previous work [66]. The catalyst for CNT growth was patterned on a silicon wafer with 300 nm of thermally grown silicon dioxide by lift-off processing using photolithography, followed by ultrasonic agitation in acetone. The catalyst layer, 10 nm of Al_2O_3, and 1 nm of Fe, were sequentially deposited by electron-beam physical vapor deposition. After dying, the wafer was placed in the quartz-tube furnace (Thermo Fisher Minimite, Waltham, WA, USA, 22 mm inner diameter) for CNT growth. The typical growth rate was ∼100 µm/min. After the growth, the furnace was cooled down to temperatures lower than 100 °C with the same gas flow and finally purged with 1000 sccm of He for 5 min. A custom-built cylindrical reactor was used to perform iCVD polymerization. The growth substrate was placed on the reactor stage above which Chromalloy filaments (Goodfellow), were held to heat the initiator (tert-butyl peroxide, TBPO, 98%, Aldrich, St. Louis, OH, USA) during polymerization. 1H,1H,2H,2H-perfluorodecylacrylate (PFDA, 97%) and the TBPO (98%) initiator were used as received from Sigma-Aldrich. The filament was heated up to 250 °C and, the labile peroxide bond of the TBPO breaks and creates −TBO radicals. The PFDA monomer was vaporized, which was then introduced to the reactor. During polymerization, the growth substrate was maintained at 30 °C with a deposition rate of 1 nm/min to ultimately coat the CNT samples with ∼30 nm thick pPFDA conformally without compromising the porosity of the CNTs. The resulting samples are nanoporous pPFDA-coated CNT forest (CF), and nanoporous microstructured pPFDA-coated CNT pillars with various diameters (D), spacings (S), and heights (H).

2.2. Spray Coated Surface Preparation

Silicon substrates were rinsed with fresh water and allowed to dry thoroughly. The samples were then treated with the two different commercial sprays (WX2100™ Cytonix, an aerosol version of Fluorothane™, and Rust-Oleum® NeverWet Liquid Repelling Treatment), which deposited the anti-wetting solutions. The sprayed samples were placed under a fume hood at lab temperature (≈22 °C) for 5 h to dry. After the solvent of the WX2100 solutions evaporated, nanoparticles coated the substrates, making them superhydrophobic. After the solvent of the NeverWet spray (acetone) evaporated, microparticles coated the substrates resulting in liquid-repelling surface.

2.3. Droplet Impact Experiment

The samples were placed on a horizontal Peltier plate, above which 9 µL water droplets (radius, $R_0 \approx 1.3$ mm) were generated by pumping liquids through a steel needle using a ramé-hart Automated Dispensing System (p/n 100-22) with accuracy of ±0.002 µL. Throughout the experiments, a needle (26 gauge with an inside diameter (ID) of 0.256 mm) was used to release the water droplets. The droplets fall on various samples with impact velocity of v = 1 m/s. Drop Volume Control software (version 10) was used to purge the dispensing systems and to control the liquid input and output.

2.4. Condensation Experiment

The surface temperature of the samples was controlled by placing them on a cooling stage (Liquid Cooled Solid State Cold Plate—LHP-1200CP, TECA Corp., Chicago, IL, USA). The bottom of the cold plate was attached to the connecting pipes through which cold Propylene Glycol was circulating by a chiller (Thermo Scientific NESLAB RTE-7 Circulating Bath). Figure S1 (see Supplementary Materials) shows test setup for the condensation. A PID Temperature Controller (TC-3400, Thermoelectric, Chicago, IL, USA) provided tighter control for demanding temperature of the Peltier plate. A T-type thermocouple was attached on the Peltier plate to measure the temperature of the plate. The thermocouple was connected to a data logging thermometer (REED SD-947 SD Series, Wilmington, NC, USA) to measure the temperature in real-time. The temperature of a sample surface became close (slightly higher such as 0.1–0.2 °C) to the temperature of the Peltier plate. This statement was verified by measuring the sample surface temperature using a non-contact Infrared Thermometer (Southwire 30010S, Carrollton, TX, USA), results of which are not shown here. The temperature and humidity of the environment were measured by Thermo-Hygrometer (General EP8703, Secaucus, NJ, USA), which also displayed the dew point for the current condition. The applied wind was created by attaching a poly-vinyl chloride (PVC) tube with Airgas Ultra High Purity nitrogen gas cylinder. The wind speed was measured using an airflow meter (Extech Thermo-Anemometer, Nashua, NH, USA) attached to an anemometer vane probe.

2.5. Contact Angle Measurement

The static (θ_c), advancing (θ_a), and receding (θ_r) contact angles of the water droplets were measured on the samples using the sessile drop technique with the help of contact angle tool from Fiji-ImageJ software (version 1.51w). A 5 µL droplet was deposited using the ramé-hart Automated Dispensing System (p/n 100-22) for static contact angle (θ_c) measurement. The advancing and receding contact angles (θ_a and θ_r) were measured by depositing water droplets of 10 µL on the surfaces, then increasing the volume by 2 µL increments until advancement in the liquid meniscus was observed and then decreasing the volume by the same rate until receding motion was seen. Advancing (θ_a) contact angle was considered as the maximum angles observed during the droplet growth, while receding contact angle (θ_r) was calculated from fitting of the drop profile just before the interface receded. To ensure repeatability, each contact angle value was averaged from measurements of ten droplets distributed across each sample. These measurements were performed at general laboratory environmental conditions (temperature of ≈22 °C and relative humidity of ≈40%).

2.6. Imaging

A FEI QUANTA 3D FEG SEM was used for obtaining the images of various samples. The spray-coated samples were coated with 10 nm of gold (Ted Pella 108 Manual Sputter Coater, Redding, CA, USA) and then images were obtained using a 2-kV acceleration voltage. Microscopy images were acquired using Leitz Ergolux microscope equipped with Infinity 2 camera. Lumenera INFINITY ANALYZE software (version 7.0.2) was used to capture the images. A high-speed video camera (OLYMPUS i-SPEED TR, Woburn, UK) was used to capture slow motion impacts of the droplets at 10,000 frames per second (FPS). Both Fiji-ImageJ and i-SPEED Viewer (version 3.1.0.9) were used for analyzing the droplet impacts. The transition of the deposited water droplet to the ice was captured using a Digital single-lens reflex (DSLR) camera (Nikon D5500, Minato City, Japan) with a macro lens (Tamron AF 90mm f/2.8 Di SP AF/MF 1:1, Saitama, Japan) for measuring the freezing delays.

3. Results and Discussion

SEM images of the samples were acquired to examine their surface features. The SEM images of the commercially available spray-coated samples (WX2100 and NeverWet) are shown in Figure S2 (see Supplementary Materials). Figure S2a shows a WX2100 coated

surface that contains nanoparticles with 100–150 nm in size on it. However, aggregates of colloidal beads with typical sizes of 5–10 μm are present on the NeverWet coated surface, indicating the presence of microtextures on the surface (Figure S2b). Figure S3a (see Supplementary Materials) shows SEM images of the nanoporous pPFDA-coated CNT forest (CF) and the nanoporous microstructured pPFDA-coated CNT pillars (CP1) surfaces. The samples have an areal density of 300 CNTs/μm^2, with individual CNTs having a mean diameter of 9 nm as-grown and 70 nm after the pPFDA coating. It is important to note conformality of the iCVD polymerization that enables maintaining the nanoporous nature of the CNTs after pPFDA deposition. Patterning of the catalyst layers by photolithography enabled fabrication of nanoporous microstructured pPFDA-coated CNT micropillars with varying diameters (D), spacings (S), and heights (H) [66]. In summary, the commercially available coating NW has microscale features, WX and the fabricated pPFDA-coated CNT forest (CF) have nanoscale features, and the pPFDA-coated CNT micropillars have both microscale and nanoscale surface features.

The static (θ_c), advancing (θ_{adv}), and receding (θ_{rec}) water contact angles on all samples (NW, WX, CF, and CP) are shown in Table S1 (see Supplementary Materials). Due to presence of surface features on all samples and their low surface energy, all samples showed superhydrophobicity with very high advancing contact angle ($\theta_{adv} > 150^\circ$) and very low contact angle hysteresis, which is the difference between advancing and receding contact angles ($(\theta_{adv} - \theta_{rec}) < 10^\circ$). In addition, droplet dynamics on all samples were examined using water droplets 1.2 mm in radius, impacting them with velocity of 1 m/s. During the droplet-impacting experiments, the substrate temperatures (T_S) were similar to the room temperature ($T_R = T_S = 22\ ^\circ C$) and the relative humidity (RH) of air was measured to be 60%. All samples demonstrated high water repellency at room temperature as the droplets were bouncing off the surfaces without any impalement (see Figure S4 and Supplementary Movie S1). In order to examine the effects of a cold and humid environment on droplet dynamics, another set of experiments were conducted.

3.1. Droplet Dynamics in Low Temperature and High Humidity Conditions

Figure S1 shows schematic of a simple setup used for conducting droplet dynamics at low temperature and high humidity conditions. The sample temperature was kept at 2 °C for 30 min and the similar droplet-impacting experiments were conducted on all samples (Figure 1). Soon after going to temperature below the dew point, the condensate water droplets started to form on all samples. After 30 min, the commercial WX and NW coating and the nanoporous pPFDA-coated CNT (CF) samples exhibited impaired water droplet bouncing on them. Upon impact, the droplets spread on these samples with a tendency to bounce off but ultimately stuck to them, resulting in impalement and their complete wetting (see Supplementary Movie S2). This could be due to penetration of the condensate water droplets into the air pockets that existed between surface textures. However, on the nanoporous microstructured CNT pillars (CP1 samples), in spite of the existence of condensate water droplets, the impacting droplet totally bounced off the surface, as shown in the bottom-row and rightmost column in Figure 1. The condensate droplets on the CP1 were observed to be on the top of the micropillars, and between them. However, the air pockets still were not completely flooded, which led them to demonstrate water repellency nature, even in condensation environments. The air pockets form a physical barrier between the nanoporous microstructured surfaces and the impacting droplet. Therefore, unlike other samples, the droplet encounters only the top of the pillars while the air pockets are still unimpaired, causing the droplet to bounce off the CP1 surfaces (Figure 1). Nevertheless, the condensate droplets on the microstructured surfaces might also cause the impalements of the impacting water droplet. In the following section, we examine the performance of various microstructured samples and compare them with the commercial WX and NW coatings.

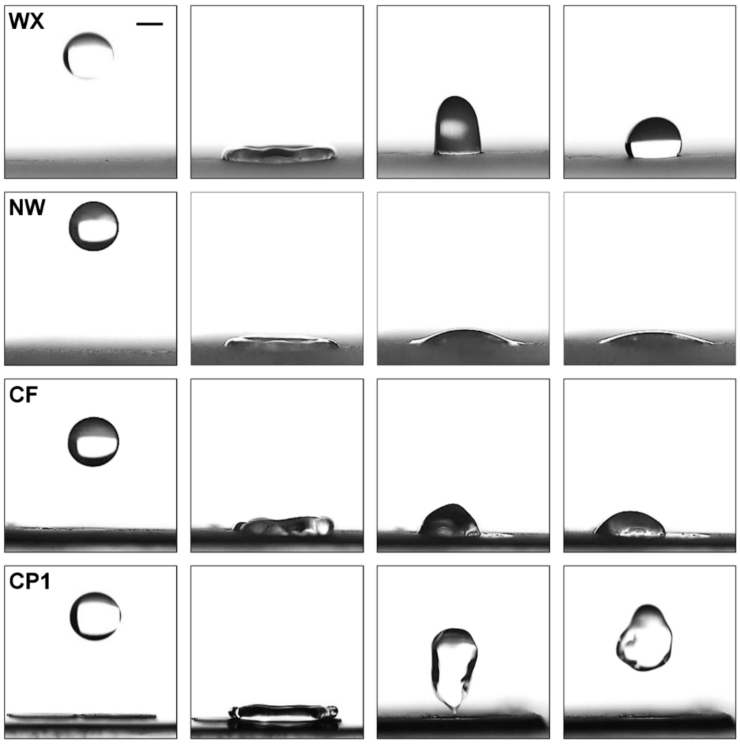


Figure 1. Sequential images showing droplets impacting various superhydrophobic surfaces at condensing environment (room temperature of T_R = 22 °C, surface temperature of T_S = 2 °C, relative humidity of RH = 60%, condensation time of 30 min, impacting velocity of droplet, v = 1 m/s, and droplet volume of V = 7.5 µL). The incoming droplets did not rebound completely after impacting commercial WX2100 (WX), NeverWet (NW), and pPFDA-coated CNT forest (CF) surfaces, whereas the droplet rebounded completely from the pPFDA-coated CNT micropillars (CP1). The scale bar is 2 mm.

3.2. Retention of Hydrophobicity in Condensate Environment

Figure 2a shows the SEM image of a nanoporous microstructured pPFDA-coated CNT surface with the pillar diameter of D, spacing of S, and height of H. Solid area fractions for solid pillars (Φ_{solid}) are determined from the following relation:

$$\Phi_{solid} = \frac{\pi D^2}{4(D+S)^2} \quad (1)$$

Table 1. The dimensions and solid area fractions (Φ) of various pPFDA-coated CNT micropillar samples. Pillar diameter (D), pillar center-to-center spacing (S), and pillar height (H).

Samples	Diameter D (µm)	Spacing S (µm)	Height H (µm)	Solid Area Fraction Φ_{solid} (%)	Actual Solid Area Fraction Φ (%)
CP1	100	30	120	46.47	11.29
CP2	70	30	120	38.48	9.35
CP3	60	40	120	28.27	6.87
CP4	50	50	120	19.64	4.77
CP5	100	30	60	46.47	11.29

Initially, the solid area fractions of the solid micropillars (taken as non-porous) were calculated. However, the CNT micropillars were highly porous with a density fraction of 0.243, mentioned in our previous work [66]. Multiplying the density fraction of 0.243 to the apparent solid pillar area fractions (Φ_{solid}), the actual solid area fractions (Φ) of the CNT micropillar samples were calculated. The dimensions along with the solid area fractions of various nanoporous CNT Pillar samples are mentioned in Table 1.

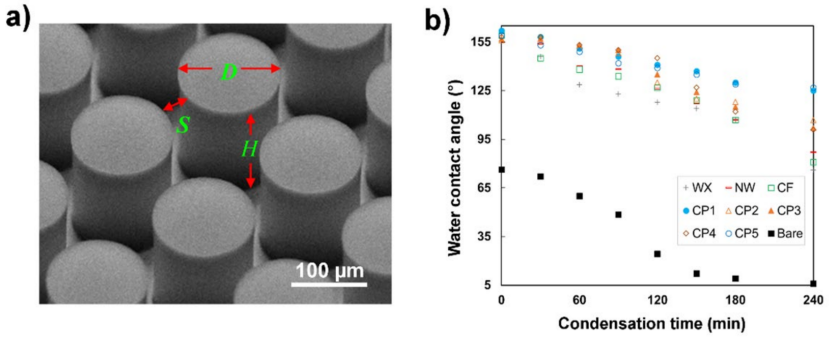


Figure 2. (**a**) SEM image of a pPFDA-coated nanoporous microstructured surface (CNT micropillars) with diameter (*D*), spacing (*S*), and height (*H*) of the micropillars. Dimension for each sample is given in Table 1. (**b**) Water contact angles (θ_c) vs. condensation time on various samples with surface temperature of T_s = 2 °C and relative humidity of *RH* = 60%. Droplet sizes for the WCA measurements were all 5 µL.

In order to examine the superhydrophobicity of our samples under various condensation degrees, the real-time water contact angles (θ_c) on them were measured. It was observed that similar deposited drops on different samples spread differently under the same condensation environments. We tested a droplet of 5 µL deposited on the NW, WX, CF, CP1, CP2, CP3, CP4, CP5, and bare silicon samples with the condensation environment at room temperature of 22 °C and relative humidity of 60%. The substrate temperature was kept at 2 °C for all the surfaces and condensate drops started to form on them. The contact angles (θ_c) of the deposited droplet on the above-mentioned samples at various condensation times were plotted and shown in Figure 2b. The water contact angle (θ_c) on the dry bare silicon sample was found to be θ_c = 76.4°. All other samples initially demonstrated superhydrophobicity, having high static water contact angles (θ_c > 150°). Under the oversaturated vapor condition, the progressive nucleation and coalescence events wetted the surfaces, resulting in reduction of the measured water contact angles. Bare silicon sample was flooded with filmwise condensation, but all other samples showed dropwise condensation. After 240 min, the WX, NW, and CF exhibited contact angles (θ_c) less than 90°, indicating a drastic loss of their hydrophobicity. The condensate droplets became larger than the roughness of these surfaces, inducing Wenzel state wetting.

The nanoporous microstructured pPFDA-coated CNT micropillars (CP1, CP2, CP3, CP4, and CP5) demonstrated reduced water contact angles as well. However, after 120 min of condensation, the surfaces with the largest solid area fraction (CP1 and CP5) demonstrated a gradual reduction of the contact angle, while other surfaces with smaller solid area fractions (CP2, CP3, and CP4) demonstrated more drastic reduction in contact angle. After 240 min of condensation, water contact angles (θ_c) for CP1 and CP5 became 125–130°, while the water contact angles (θ_c) on CP2, CP3, and CP4 became as low as 100–106°. Although all the CNT micropillar surfaces lost their superhydrophobicity, having the contact angles (θ_c) less than 150°, they still retained their hydrophobicity even after 240 min. CP1 and CP5 showed better retention in hydrophobicity due to their higher solid area fraction (Φ = 11.29%) compared to the remaining surfaces with smaller solid area fractions CP2 (9.35%), CP3 (6.87%), and CP4 (4.77%). To understand the effect of solid area fraction on hydrophobicity retention, we studied the coalescence of the condensate droplets on micropillars with different features.

3.3. Condensation and Coalescence on CNT Micropillars

To understand the relation between the geometry of micropillars and the condensation growth on them, condensation experiments were conducted on the various CNT micropillar surfaces. Figure 3a shows the comparison of the coalesced condensates on the CNT micropillars with the smallest solid area fraction (CP4) and the largest solid area fractions (CP5) after 180 min of condensation. For CP4, the droplets on the top of the pillars

coalesced with the droplets in the cavities and got sucked in, resulted in large Wenzel droplets (Figure 3a(i)). Coalesced condensate droplets further grew, coalesced, and finally overgrew on the CNT micropillars by flooding them. For CP5 though, the droplets inside the cavities coalesced with the droplets on the tops, resulting in a large coalesced droplet at the top of the center pillar (Figure 3b(ii)). The overgrown larger droplets formed a non-wetting Cassie–Baxter state without any pinning on the base. Micropillars CP2 and CP3 with smaller solid area fractions than CP5 showed coalescence of condensates similar to CP4. Therefore, the condensate micro drops should be in the scale of the pillars to be able to overgrow on the top of the micropillars and be in Cassie-Baxter state after coalescence.

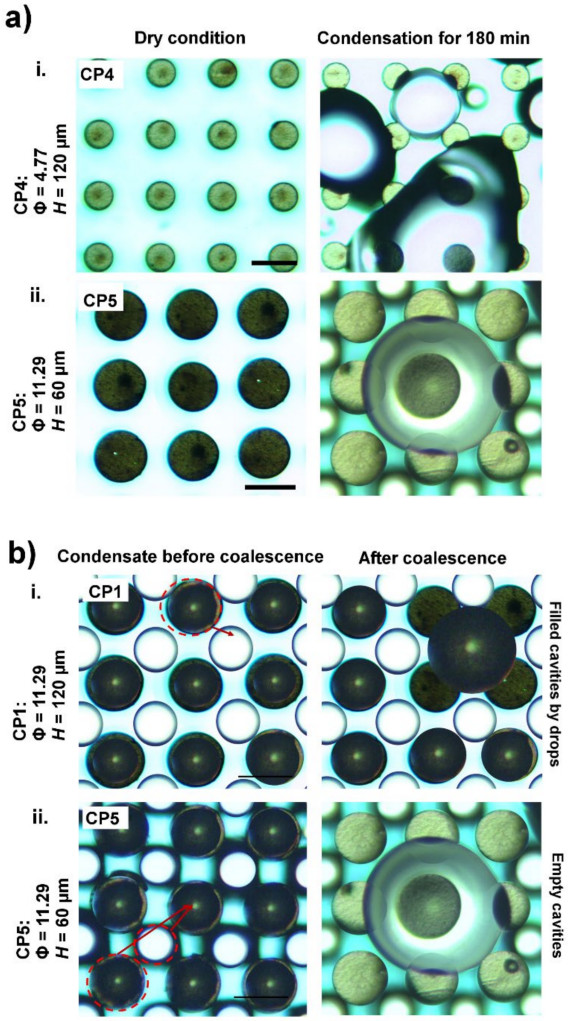


Figure 3. Growth behavior of the condensate droplets on the pPFDA-coated CNT micropillars with varying solid area fractions (Φ) in a) and with varying micropillars heights (*H)* in b). (**a**) Images exhibiting the overgrowth of the condensate droplets on the CP4 (**i**) and CP5 (**ii**) substrates after 180 min of condensation from the dry condition (left side). Condensate droplets grew and coalesced forming Wenzel state on CP4. In contrast, condensate droplets grew and formed non-wetting Cassie–Baxter state on CP5. (**b**) Images showing the effect of micropillar heights on coalescence behavior of the condensate droplets on the pPFDA-coated CNT micropillars (**i**) CP1: H = 120 μm, and (**ii**) CP5: H = 60 μm). Spheres inside dashed circle are condensate droplets. On the CP1 sample, the micro droplets only on the tops coalesced together. In contrast, coalescing of micro droplets both from tops and cavities into a single droplet occurred on the tops of the micropillars of the sample CP5. The micro droplets from cavities overgrew on the tops, making the cavities empty. The scale bars both in (**a**,**b**) represent 100 μm.

To understand the coalescence of the condensate drops on the CNT micropillars with the similar high solid area fraction but with different heights, we investigated the moments before and after the coalescence incidents both on CP1 and CP5 (Figure 3b). While having the similar high solid area fraction (Φ = 11.29%), the CP5 sample contained micropillars with half of the height (H = 60 μm) compared to the micropillars of CP1 (H = 120 μm). On the sample CP1, the micro drops on the tops coalesced together. The micro condensate drops in the cavities, being smaller than the micropillar height, could not reach out the drops on the top of the pillars (Figure 3b(i)). Thus, the drops in the cavities remained there. In contrast, condensate drops from both tops and cavities coalesced into a single droplet on the tops of the micropillars on CP5, as shown in Figure 3b(ii). The micro droplets from cavities overgrew on the tops, making the cavities empty. Thus, the coalesced drops remained in Cassie-Baxter state on both CP1 and CP5. However, the cavities were partially filled by condensate droplets on CP1, but the same were empty on CP5 after the coalescence, which played a significant role in heat transfer, i.e., in delaying freezing of water droplets on the nanoporous microstructured surfaces during freezing conditions. A numerical or calculative analysis for theorizing a threshold height for allowing easy coalescence of the droplets is a potential scope for future study.

3.4. Delay in Freezing of Water Droplets

Experiments were conducted for checking the icephobicity of the various superhydrophobic surfaces (WX, NW, CF, CP1, CP2, CP3, CP4, and CP5) in terms of freezing delays. The freezing delay experiments were divided into two categories. At first, we conducted the direct-freezing delay experiments where the sample was directly placed on the Peltier plate with temperature of −10 °C and then a 9 μL water droplet was deposited on the cold samples. The droplet freezing moment was visually observed by a change in the transparency of the water droplet from a clear state to an opaque state, as shown in Figure 4a. Freezing delays were measured by deducting the freezing time of the droplet on a bare silicon sample from freezing time of the droplet on the superhydrophobic samples. The number of trials were three. On the various samples, the freezing delay times were measured for the microdroplet (9 μL) and the comparison is provided in Figure 4b(i). (patterned blue columns). All the freezing delay values for the direct-freezing condition are given in Table S2 (see Supplementary Materials).

CNT micropillars demonstrated better icephobicity in regard of freezing delays than other samples with micro or nano roughness (WX, NW, and CF). This is due to the higher thermal barrier resulting from the high volumes of air pockets in nanoporous microstructured surfaces. Among the CNT micropillars, the samples having the smaller solid area fractions demonstrated higher freezing delays, due to the lower contact area between droplet and the cold surfaces. For the CNT micropillars having a similar solid area fraction, the sample with the higher pillar height (CP1) demonstrated longer freezing delays than the sample with lower pillar height (CP5). A potential explanation for this phenomenon could be that the bigger air pockets acted as a larger thermal barrier [67]; thus, the delayed freezing of the water droplets occurred.

In the second set of freezing delay experiments, the temperature of the samples was initially kept in condensation environment (at 5 °C) for 180 min and a gentle wind with velocity of 0.5 m/s was blown across them. As shown in Figure 3b, the coalesced drops maintained Cassie-Baxter state on CP1 and CP5. Thus, they were easily removed by the applied wind. However, the coalesced droplets stuck in cavities and the Wenzel drops remained on CP2, CP3, and CP4, and were not removed upon the gentle wind. The coalesced condensate drops filled the cavities or air pockets even after the wind was applied. Though the deposited droplets on commercial coatings WX and NW along with CNT forest (CF) showed drastic contact angle (θ_c) reduction due to condensation, the coalesced condensate drops maintained the Cassie state on them. Thus, most of the condensate drops on them got removed by the applied wind. The temperature of all these samples were then decreased to −10 °C for conducting the freezing delay experiments after

the condensation. The decreasing trend of the surface temperature from the condensation condition to the freezing condition is shown as a plot in Figure 4b(ii).

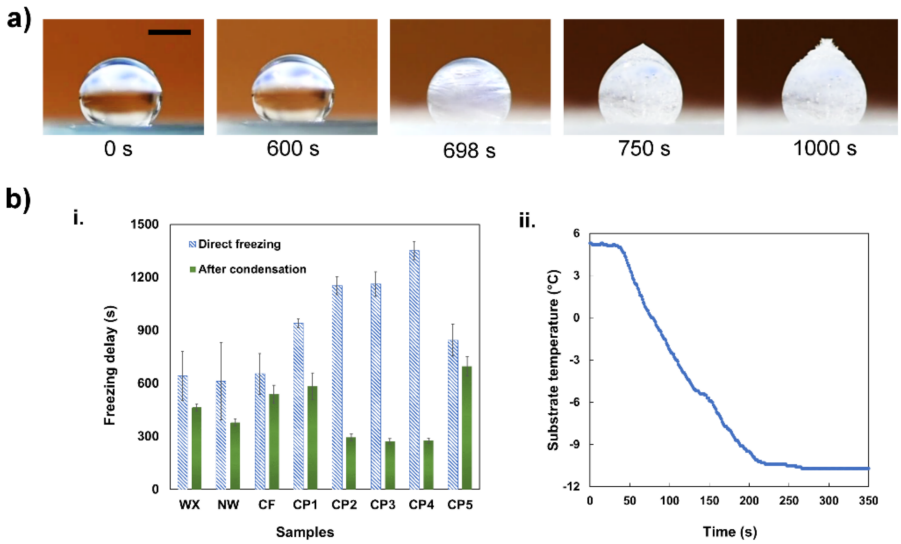


Figure 4. (**a**) Images showing the change in transparency of a droplet during freezing on a pPFDA-coated CNT micropillars (CP5). Change in the morphology of a 9 µL droplet as a function of time during cooling. Condensation began at 5 °C and led to freezing at −10 °C. The scale bar represents 2 mm. (**b**) (**i**) Freezing delays on various samples by direct freezing (patterned blue column) and freezing followed by condensation (solid green column). (**ii**) Plot showing the cooling curve on substrates when the temperature was reduced from the condensation temperature of 5 °C to the freezing temperature of −10 °C.

The freezing delay values for the freezing following condensation experiments were plotted and shown in Figure 4b(i) (solid green columns). All the freezing delay values on the various samples for the freezing following condensation experiments are given in Table S2 (see Supplementary Materials). The reduction in freezing delays was not significant for the WX, NW, and CF samples due to the removal of the Cassie state condensates by the gentle wind. As for the CNT micropillars, there were interesting changes in the freezing delays. While having the highest freezing delays in direct freezing experiments, the CNT micropillars with the smaller solid area fractions (CP2, CP3, and CP4) demonstrated the lowest freezing delays in the condensation followed by freezing condition. The freezing delays were found to be 1153 ± 50 s, 1162 ± 70 s, and 1351 ± 50 s for the direct freezing on the CP2, CP3, and CP4 samples, respectively. Whereas the freezing delays after condensation on the same samples decreased to 295 ± 25 s, 273 ± 15 s, and 276 ± 15 s, respectively. On the other hand, the CNT micropillars with the highest solid area fraction (CP1 and CP5) still demonstrated better icephobicity in respect of showing higher freezing delays. However, there is a greater reduction in freezing delay for droplets on the CP1 compared to the same for CP5. The CP5 sample, having the same solid area fraction as CP1 but height as half as the same of CP1, it showed a minimal reduction in freezing delays for the condensation followed by freezing condition compared to direct freezing condition. The freezing delays for direct freezing were 941 ± 25 s and 845 ± 90 s on the CP1 and CP5 samples, respectively. Whereas the freezing delays after condensation freezing were 585 ± 75 s and 701 ± 55 s on the CP1 and CP5 samples, respectively. This distinction of reduction in freezing delays can be explained by understanding the coalesced condensates on both surfaces. As shown previously in Figure 3b, the drops in the cavities could not overgrow on the top of the micropillars on CP1. However, the drops coalesced and overgrew on the top of the pillars on CP5. Therefore, the air pockets became empty when coalesced condensate drops were removed from the CP5 by the gentle wind, which was not the case for the CP1 sample, as shown in Figure 5a. The tiny micro droplets seen on air pockets of the CP5 samples are the

condensates that grow right after removal of the bigger droplets. After the removal of the drops on the top by the wind, there were still large, coalesced drops between the pillars of CP1. When the temperature went down, the partially filled cavities on CP1 increased the heat transfer between the deposited droplet and the surface. Whereas the air pockets on the CP5, being empty and not significantly impaired, still acted as an efficient thermal barrier between the incoming droplet and the surface. As shown in Figure 5b, the drops at the cavities froze on CP1 (left side), whereas the cavities are clear of ice in CP5 (right side). In the following section, the durability of sample CP5, which performed well in delaying ice formation, is illustrated.

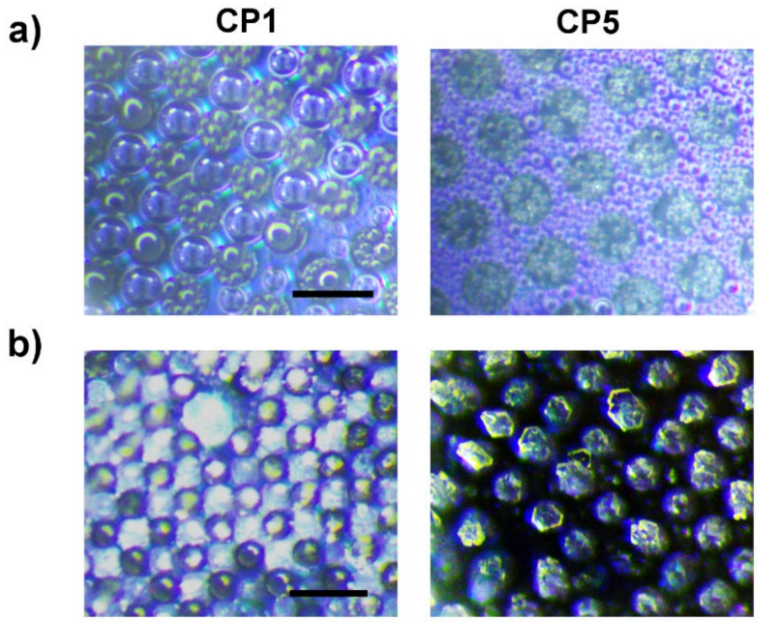


Figure 5. Images showing the condensate droplets after removal of the large, coalesced condensate drops (**a**) and after subsequent freezing (**b**). (**a**) Different condensate states on the pPFDA-coated CNT micropillars with same solid area fraction (Φ) but different pillar heights (H) (CP1 and CP5) after condensation and removal of the coalesced condensate drops by the gentle wind. The scale bar is 200 μm. (**b**) Air pockets were filled with frozen condensate droplets on CP1, while the same were empty on CP5 when the temperature of these samples went down from condensation temperature of 5 °C to the freezing temperature of −10 °C. These distinct conditions of the air pockets on CP1 and CP5 samples eventually determined the different freezing delays. The scale bar is 300 μm.

3.5. Durability of CP5

Several icing/de-icing cycles of experiments were conducted on the CNT micropillar sample CP5. Contact angle (θ_c) and contact angle hysteresis ($\theta_{adv} - \theta_{rec}$) values were measured on the sample between the icing/de-icing experiments, and the results are presented in Figure 6 as a function of the number of icing/de-icing events. After a considerable amount of cycles, the CNT micropillar sample still retained its hydrophobicity by showing high water contact angle (θ_c) and low contact angle hysteresis ($\theta_{adv} - \theta_{rec}$). Previous studies demonstrated that the anti-wetting property deteriorates after several icing/de-icing cycles [37,45]. Damages occurred by the icing process due to the water expansion on the solid surface caused by freezing, inducing significant interfacial stress [37,45]. In our case, the extremely high porosity and elasticity of the CNTs prevented the significant interfacial stress and provided sustainability over the freezing cycles.

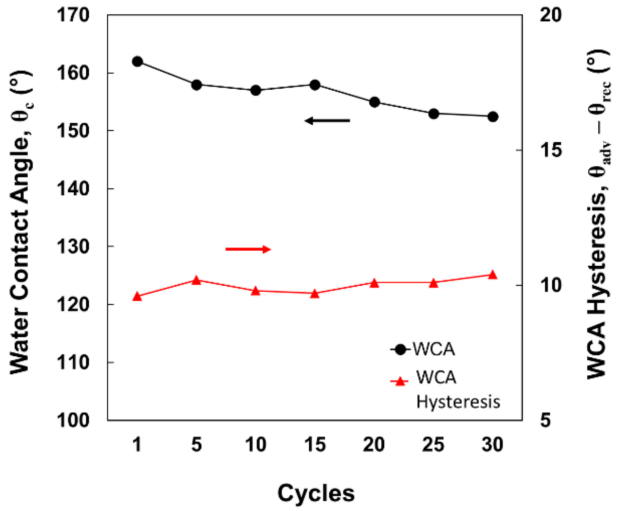


Figure 6. Water contact angle (θ_c) and contact angle hysteresis ($\theta_{adv} - \theta_{rec}$) after icing/de-icing cycles on the pPFDA-coated CNT micropillar (CP5).

4. Conclusions

In summary, we investigated the characteristics of condensation forming on the various fabricated pPFDA-coated nanoporous microstructured surfaces and commercially available hydrophobic coatings. Condensation leads to an invasion of the surface roughness and to the formation of both Cassie, Wenzel, and filmwise states. Highly porous CNT micropillars with higher solid area fraction demonstrated better performance in condensation and freezing following condensation environments. When the sizes of the micropillars were in the scale of the drops in the cavities, the drops in the cavities overgrew and formed Cassie state after coalescing with the condensate drops on the top of the micropillars, which were removed by a gentle wind. Thus, the CNT micropillars retained their hydrophobicity even after considerable amount of time in condensation environments, having their air pockets not filled by the condensate drops. When the temperature of the micropatterned sample with highest solid fraction, but lower height went down from condensation temperature to the freezing temperature, the air pockets of the sample were empty. This desirable condition of the air pockets on the micropatterned samples induced larger freezing delays compared to samples with lower solid area fractions and higher heights. This facilitated the nanoporous CNT micropillars with appropriate geometry to retain icephobicity in the condensation followed by freezing conditions. High porosity of CNTs provided durability in multiple icing/de-icing cycles as well. These approved the nanoporous microstructured superhydrophobic surfaces being a potential candidate for preventing condensation and ice in harsh conditions. This study enables a better understanding of the wetting states of the condensate droplets along with the freezing phenomena that occurred on the highly porous superhydrophobic microstructured CNTs, which will help designing engineered surfaces with optimized textures for the practical use of them in humid and low temperature environments.

Supplementary Materials: The following are available online at https://www.mdpi.com/article/10.3390/coatings11060617/s1, Figure S1: Experimental setup. The sample was placed on a PID-controlled Peltier plate, which sits on a horizontal stage. Cold Propylene Glycol circulated inside pipes connected to the Peltier plate by a chiller. The sample was illuminated by a cool LED lighting and images were captured by camera above condensation. Figure S2: Images of spray coatings. Scanning electron microscope images of the commercial anti-wetting spray coatings deposited on a silicon substrate. (a) SEM images of a substrate coated by WX2100 spray, inset: close-up view of the texture with nanoparticles of 100–150 nm. (b) SEM im-age of a substrate coated by NeverWet spray with aggregated colloidal beads with typical sizes of 5–10 μm. Figure S3: Carbon nanotube samples. (a) SEM images of the pPFDA-coated carbon nanotube for-est. Tilted (left) and top view (right) show-

ing the roughness on the top of the CNT forest. (b) SEM images showing nanoporous microstructured pPFDA-coated CNT micropillars (CP1), where each micropillar consisted of highly porous CNTs. Top and side views are also shown to demonstrate their high porosity, along with presence of features at different length scale. Figure S4: Droplet impacting on different superhydrophobic surfaces WX2100 (WX), NeverWet (NW), pPFDA-coated CNT Forest (CF) and pPFDA-coated CNT Pillars (CP1) at experimental conditions of room temperature TR = 22 °C, surface temperature TS = 22 °C, relative humidity RH = 60%, impacting velocity of droplet, v = 1 m/s, droplet volume, V = 7.5 µL. All of them demonstrated high water repellency at room temperature as the droplets bounce off the surfaces without any impalement/sticking. The scale bar is 2 mm. Table S1: Static (θ_c), advancing (θ_a), and receding (θ_r) water contact angles on commercial NeverWet (NW) and WX2100 (WX) coatings and pPFDA-coated CNT forest (CF) and CNT micropillars (CP1), Table S2. Freezing delays on various samples for direct freezing conditions and condensation then freezing conditions. Movie S1: Water droplet bouncing at dry condition. The four different samples (NeverWet (NW), WX2100 (WX), pPFDA-coated CNT Forest (CF) and pPFDA-coated CNT micropillars (CP1) are exposed to the water droplet (radius R = 1.2 mm) impacting on the surfaces with impact velocity v = 1 m/s. The substrate temperatures are close to the room temperature 22 °C and the relative humidity (RH) of environment is 60%. The four various samples demonstrate high water repellency at room temperature as the droplets bounce off the surfaces without any impalement. Movie S2: Water droplet bouncing at condensation condition. The four different samples (NeverWet (NW), WX2100 (WX), pPFDA-coated CNT Forest (CF) and pPFDA-coated CNT micropillars (CP1) are exposed to the water droplet (radius *R* = 1.2 mm) impacting on the surfaces with impact velocity v = 1 m/s. The room temperature is 22 °C and relative humidity (RH) is 60%. The samples are placed on a Peltier cooling stage to condense atmospheric vapor on them and make them wet. The substrate temperature is kept at 2 °C for 30 min before conducting the droplet impacting experiments. The impacting droplets encounter and spread on the surfaces, try to bounce off but stick to them, resulting in impalement and a complete wetting on the WX, NW and CF samples. However, the impacting droplet totally bounces off the CP1 surface. Movie S3: Comparison of freezing delays for the freezing following condensation conditions on bare silicon, pPFDA-coated CNT micropillars CP1 and CP5. The room temperature is 22 °C and relative humidity (RH) is 60%. The samples are initially placed at 5 °C for 180 min and then a gentle wind velocity of 0.5 m/s is applied on them. The contact angles (θ_c) of the deposited droplets are 14.5°, 133.6°, and 136.1° for the bare silicon, CP1, and CP5, respectively. The temperatures of all these samples are then decreased to −10 °C for conducting the freezing delay experiments after condensation for determining the freezing time of water droplets (12 µL) by observing the change in transparency of the droplet during freezing. The freezing times are 25, 585 and 701 s for the bare silicon, CP1 and CP5 samples, respectively.

Author Contributions: Conceptualization, H.S. and A.R.; Formal analysis, A.R.; Investigation, B.M.; Methodology, H.S., A.R., and B.M.; Project administration, H.S. and A.R.; Supervision, H.S.; Validation, B.M.; Writing—original draft, A.R.; Writing—review & editing, H.S., and B.M. All authors have read and agreed to the published version of the manuscript.

Funding: This research received no external funding.

Institutional Review Board Statement: Not applicable.

Informed Consent Statement: Not applicable.

Acknowledgments: The authors thank Karen K. Gleason and Minghui Wang, Department of Chemical Engineering, Massachusetts Institute of Technology (MIT) for iCVD polymer deposition and A. John Hart and Sanha Kim, Department of Mechanical Engineering, Massachusetts Institute of Technology (MIT) for providing the CNT samples.

Conflicts of Interest: The authors declare no conflict of interest.

References

1. Nakajima, A.; Hashimoto, K.; Watanabe, T. Recent studies on super-hydrophobic films. *Mon. Fur Chem.* **2001**, *132*, 31–41. [CrossRef]
2. Jung, Y.C.; Bhushan, B. Dynamic effects of bouncing water droplets on superhydrophobic surfaces. *Langmuir* **2008**, *24*, 6262–6269. [CrossRef] [PubMed]

3. Richard, D.; Clanet, C.; Quéré, D. Surface phenomena: Contact time of a bouncing drop. *Nature* **2002**, *417*, 811. [CrossRef] [PubMed]
4. Quan, Y.; Zhang, L.-Z. Numerical and analytical study of the impinging and bouncing phenomena of droplets on superhydrophobic surfaces with microtextured structures. *Langmuir* **2014**, *30*, 11640–11649. [CrossRef]
5. Shen, Y.; Tao, J.; Tao, H.; Chen, S.; Pan, L.; Wang, T. Relationship between wetting hysteresis and contact time of a bouncing droplet on hydrophobic surfaces. *ACS Appl. Mater. Interfaces* **2015**, *7*, 20972–20978. [CrossRef]
6. Yin, L.; Zhang, H.; Weng, R.; Wu, Z.; Liu, X. Fabrication and drag reduction of the superoleophobic surface on a rotational gyroscope. *Surf. Eng.* **2018**, *34*, 165–171. [CrossRef]
7. Yao, H.; Zhou, X. A pioneering method for reducing water droplet erosion. *J. Fluids Eng.* **2018**, *140*, 61401. [CrossRef]
8. Sojoudi, H.; Wang, M.; Boscher, N.D.; McKinley, G.H.; Gleason, K.K. Durable and scalable icephobic surfaces: Similarities and distinctions from superhydrophobic surfaces. *Soft Matter* **2016**, *12*, 1938–1963. [CrossRef]
9. Chew, N.G.P.; Zhao, S.; Malde, C.; Wang, R. Superoleophobic surface modification for robust membrane distillation performance. *J. Memb. Sci.* **2017**, *541*, 162–173. [CrossRef]
10. Wang, N.; Xiong, D.; Deng, Y.; Shi, Y.; Wang, K. Mechanically robust superhydrophobic steel surface with anti-icing, uv-durability, and corrosion resistance properties. *ACS Appl. Mater. Interfaces* **2015**, *7*, 6260–6272. [CrossRef]
11. Ishizaki, T.; Sakamoto, M. Facile formation of biomimetic color-tuned superhydrophobic magnesium alloy with corrosion resistance. *Langmuir* **2011**, *27*, 2375–2381. [CrossRef]
12. Yong, J.; Chen, F.; Yang, Q.; Huo, J.; Hou, X. Superoleophobic surfaces. *Chem. Soc. Rev.* **2017**, *46*, 4168–4217. [CrossRef]
13. Moqaddam, A.M.; Chikatamarla, S.S.; Karlin, I.V. Drops bouncing off macro-textured superhydrophobic surfaces. *J. Fluid Mech.* **2017**, *824*, 866–885. [CrossRef]
14. Liu, Y.; Whyman, G.; Bormashenko, E.; Hao, C.; Wang, Z. Controlling drop bouncing using surfaces with gradient features. *Appl. Phys. Lett.* **2015**, *107*, 51604. [CrossRef]
15. Chen, L.; Wu, J.; Li, Z.; Yao, S. Evolution of entrapped air under bouncing droplets on viscoelastic surfaces. *Colloids Surfaces A Physicochem. Eng. Asp.* **2011**, *384*, 726–732. [CrossRef]
16. Liu, Y.; Moevius, L.; Xu, X.; Qian, T.; Yeomans, J.M.; Wang, Z. Pancake bouncing on superhydrophobic surfaces. *Nat. Phys.* **2014**, *10*, 515. [CrossRef]
17. Namdari, N.; Mohammadian, B.; Jafari, P.; Mohammadi, R.; Sojoudi, H.; Ghasemi, H.; Rizvi, R. Advanced functional surfaces through controlled damage and instabilities. *Mater. Horiz.* **2020**, *7*, 366–396. [CrossRef]
18. Sojoudi, H.; Arabnejad, H.; Raiyan, A.; Shirazi, S.A.; McKinley, G.H.; Gleason, K.K. Scalable and durable polymeric icephobic and hydrate-phobic coatings. *Soft Matter* **2018**. [CrossRef]
19. Bjornstig, U.; Bjornstig, J.; Dahlgren, A. Slipping on ice and snow—Elderly women and young men are typical victims. *Accid. Anal. Prev.* **1997**, *29*, 211–215. [CrossRef]
20. Laforte, J.L.; Allaire, M.A.; Laflamme, J. State-of-the-art on power line de-icing. *Atmos. Res.* **1998**, *46*, 143–158. [CrossRef]
21. Dalili, N.; Edrisy, A.; Carriveau, R. A review of surface engineering issues critical to wind turbine performance. *Renew. Sustain. Energy Rev.* **2009**, *13*, 428–438. [CrossRef]
22. Fillion, R.M.; Riahi, A.R.; Edrisy, A. A review of icing prevention in photovoltaic devices by surface engineering. *Renew. Sustain. Energy Rev.* **2014**, *32*, 797–809. [CrossRef]
23. Jiang, X.; Zhao, J.; Luo, B.; Zhang, J.; Huang, C. Survey and analysis of ice accidents of early 2008 in southern China. In Proceedings of the The 13th International Workshop on Atmoshperic Icing of Structures, Chongqing, China, 8–11 September 2009; pp. 1–7.
24. Zheng, L.; Shafack, R.; Walker, B.; Chan, K. The impact of high humidity on the ice-phobicity of copper-based superhydrophobic surfaces. *Nanomater. Nanotechnol.* **2017**, *7*, 1847980417707174. [CrossRef]
25. He, Z.; Vågenes, E.T.; Delabahan, C.; He, J.; Zhang, Z. Room temperature characteristics of polymer-based low ice adhesion surfaces. *Sci. Rep.* **2017**, *7*, 42181. [CrossRef]
26. Sojoudi, H.; McKinley, G.H.; Gleason, K.K. Linker-free grafting of fluorinated polymeric cross-linked network bilayers for durable reduction of ice adhesion. *Mater. Horiz.* **2015**, *2*, 91–99. [CrossRef]
27. Raiyan, A.; Mclaughlin, T.S.; Annavarapu, R.K.; Sojoudi, H. Effect of superamphiphobic macrotextures on dynamics of viscous liquid droplets. *Sci. Rep.* **2018**, *8*, 15344. [CrossRef]
28. Mishchenko, L.; Hatton, B.; Bahadur, V.; Taylor, J.A.; Krupenkin, T.; Aizenberg, J. Design of ice-free nanostructured surfaces based on repulsion of impacting water droplets. *ACS Nano* **2010**, *4*, 7699–7707. [CrossRef]
29. Schutzius, T.M.; Jung, S.; Maitra, T.; Graeber, G.; Köhme, M.; Poulikakos, D. Spontaneous droplet trampolining on rigid superhydrophobic surfaces. *Nature* **2015**, *527*, 82–85. [CrossRef]
30. Mohammadian, B.; Annavarapu, R.K.; Raiyan, A.; Nemani, S.K.; Kim, S.; Wang, M.; Sojoudi, H. Delayed frost growth on nanoporous microstructured surfaces utilizing jumping and sweeping condensates. *Langmuir* **2020**. [CrossRef]
31. Miljkovic, N.; Enright, R.; Nam, Y.; Lopez, K.; Dou, N.; Sack, J.; Wang, E.N. Jumping-droplet-enhanced condensation on scalable superhydrophobic nanostructured surfaces. *Nano Lett.* **2013**, *13*, 179–187. [CrossRef]
32. Zhang, Q.; He, M.; Chen, J.; Wang, J.; Song, Y.; Jiang, L. Anti-icing surfaces based on enhanced self-propelled jumping of condensed water microdroplets. *Chem. Commun.* **2013**, *49*, 4516–4518. [CrossRef]

33. Dorrer, C.; Rühe, J. Condensation and wetting transitions on microstructured ultrahydrophobic surfaces. *Langmuir* **2007**, *23*, 3820–3824. [CrossRef] [PubMed]
34. Narhe, R.D.; Beysens, D.A. Water condensation on a super-hydrophobic spike surface. *EPL Europhys. Lett.* **2006**, *75*, 98. [CrossRef]
35. Peng, Q.; Jia, L.; Ding, Y.; Dang, C.; Yin, L.; Yan, X. Influence of groove orientation on dropwise condensation on hydrophobic and hierarchical superhydrophobic surfaces with microgroove arrays. *Int. Commun. Heat Mass Transf.* **2020**, *112*, 104492. [CrossRef]
36. Miljkovic, N.; Preston, D.J.; Enright, R.; Wang, E.N. Electric-field-enhanced condensation on superhydrophobic nanostructured surfaces. *ACS Nano* **2013**, *7*, 11043–11054. [CrossRef]
37. Chen, T.; Cong, Q.; Qi, Y.; Jin, J.; Choy, K.-L. Hydrophobic durability characteristics of butterfly wing surface after freezing cycles towards the design of nature inspired anti-icing surfaces. *PLoS ONE* **2018**, *13*, e0188775. [CrossRef]
38. Kreder, M.J.; Alvarenga, J.; Kim, P.; Aizenberg, J. Design of anti-icing surfaces: Smooth, textured or slippery? *Nat. Rev. Mater.* **2016**, *1*. [CrossRef]
39. Oberli, L.; Caruso, D.; Hall, C.; Fabretto, M.; Murphy, P.J.; Evans, D. Condensation and freezing of droplets on superhydrophobic surfaces. *Adv. Colloid Interface Sci.* **2014**, *210*, 47–57. [CrossRef]
40. He, M.; Li, H.; Wang, J.; Song, Y. Superhydrophobic surface at low surface temperature. *Appl. Phys. Lett.* **2011**, *98*, 93118. [CrossRef]
41. Krishnan, D.V.; Kumar, G.U.; Suresh, S.; Jubal, M.; Thansekhar, M.R.; Ramesh, R. Wetting transition in laser-fabricated hierarchical surface structures and its impact on condensation heat transfer characteristics. *Int. J. Heat Mass Transf.* **2019**, *140*, 886–896. [CrossRef]
42. Enright, R.; Miljkovic, N.; Al-Obeidi, A.; Thompson, C.V.; Wang, E.N. Condensation on superhydrophobic surfaces: The role of local energy barriers and structure length scale. *Langmuir* **2012**, *28*, 14424–14432. [CrossRef]
43. Furuta, T.; Sakai, M.; Isobe, T.; Nakajima, A. Effect of dew condensation on the wettability of rough hydrophobic surfaces coated with two different silanes. *Langmuir* **2010**, *26*, 13305–13309. [CrossRef]
44. Wang, F.; Ding, W.; He, J.; Zhang, Z. Phase transition enabled durable anti-icing surfaces and its DIY design. *Chem. Eng. J.* **2019**, *360*, 243–249. [CrossRef]
45. Farhadi, S.; Farzaneh, M.; Kulinich, S.A. Anti-icing performance of superhydrophobic surfaces. *Appl. Surf. Sci.* **2011**, *257*, 6264–6269. [CrossRef]
46. Kulinich, S.A.; Farhadi, S.; Nose, K.; Du, X.W. Superhydrophobic surfaces: Are they really ice-repellent? *Langmuir* **2010**, *27*, 25–29. [CrossRef]
47. Lafuma, A.; Quéré, D. Superhydrophobic states. *Nat. Mater.* **2003**, *2*, 457. [CrossRef]
48. Quéré, D.; Lafuma, A.; Bico, J. Slippy and sticky microtextured solids. *Nanotechnology* **2003**, *14*, 1109.
49. Mariappan, D.D.; Kim, S.; Boutilier, M.S.H.; Zhao, J.; Zhao, H.; Beroz, J.; Muecke, U.; Sojoudi, H.; Gleason, K.; Brun, P.T.; et al. Dynamics of liquid transfer from nanoporous stamps in high-resolution flexographic printing. *Langmuir* **2019**, *35*, 7659–7671. [CrossRef]
50. Annavarapu, R.K.; Kim, S.; Wang, M.; Hart, A.J.; Sojoudi, H. Explaining evaporation-triggered wetting transition using local force balance model and contact line-fraction. *Sci. Rep.* **2019**, *9*, 1–17. [CrossRef]
51. Narhe, R.D.; Beysens, D.A. Growth dynamics of water drops on a square-pattern rough hydrophobic surface. *Langmuir* **2007**, *23*, 6486–6489. [CrossRef]
52. Rykaczewski, K. Microdroplet growth mechanism during water condensation on superhydrophobic surfaces. *Langmuir* **2012**, *28*, 7720–7729. [CrossRef]
53. Sun, X.; Damle, V.G.; Uppal, A.; Linder, R.; Chandrashekar, S.; Mohan, A.R.; Rykaczewski, K. Inhibition of condensation frosting by arrays of hygroscopic antifreeze drops. *Langmuir* **2015**, *31*, 13743–13752. [CrossRef]
54. Cai, L.; Wang, R.; Hou, P.; Zhang, X. Study on restraining frost growth at initial stage by hydrophobic coating and hygroscopic coating. *Energy Build.* **2011**, *43*, 1159–1163. [CrossRef]
55. Azimi, G.; Dhiman, R.; Kwon, H.M.; Paxson, A.T.; Varanasi, K.K. Hydrophobicity of rare-earth oxide ceramics. *Nat. Mater.* **2013**, *12*, 315–320. [CrossRef]
56. Hu, M.Z.; Bischoff, B.L.; Morales-Rodriguez, M.E.; Gray, K.A.; Davison, B.H. Superhydrophobic or hydrophilic porous metallic/ceramic tubular membranes for continuous separations of biodiesel-water W/O and O/W emulsions. *Ind. Eng. Chem. Res.* **2019**, *58*, 1114–1122. [CrossRef]
57. Kujawa, J.; Al-Gharabli, S.; Kujawski, W.; Knozowska, K. Molecular grafting of fluorinated and nonfluorinated alkylsiloxanes on various ceramic membrane surfaces for the removal of volatile organic compounds applying vacuum membrane distillation. *ACS Appl. Mater. Interfaces* **2017**, *9*, 6571–6590. [CrossRef]
58. Wankhede, R.G.; Morey, S.; Khanna, A.S.; Birbilis, N. Development of water-repellent organic-inorganic hybrid sol-gel coatings on aluminum using short chain perfluoro polymer emulsion. *Appl. Surf. Sci.* **2013**, *283*, 1051–1059. [CrossRef]
59. Wang, J.W.; Li, X.Z.; Fan, M.; Gu, J.Q.; Hao, L.Y.; Xu, X.; Chen, C.S.; Wang, C.M.; Hao, Y.Z.; Agathopoulos, S. Porous B-Sialon planar membrane with a robust polymer-derived hydrophobic ceramic surface. *J. Memb. Sci.* **2017**, *535*, 63–69. [CrossRef]
60. Wisdom, K.M.; Watson, J.A.; Qu, X.; Liu, F.; Watson, G.S.; Chen, C.-H. Self-cleaning of superhydrophobic surfaces by self-propelled jumping condensate. *Proc. Natl. Acad. Sci. USA* **2013**, *110*, 7992–7997. [CrossRef] [PubMed]
61. Li, T.; Ibáñez Ibáñez, P.F.; Håkonsen, V.; Wu, J.; Xu, K.; Zhuo, Y.; Luo, S.; He, J.; Zhang, Z. Self-deicing electrolyte hydrogel surfaces with pa-level ice adhesion and durable anti-freezing/frost performance. *ACS Appl. Mater. Interfaces* **2020**. [CrossRef]

62. Boreyko, J.B.; Hansen, R.R.; Murphy, K.R.; Nath, S.; Retterer, S.T.; Collier, C.P. Controlling condensation and frost growth with chemical micropatterns. *Sci. Rep.* **2016**, *6*, 19131. [CrossRef]
63. Wier, K.A.; McCarthy, T.J. Condensation on ultrahydrophobic surfaces and its effect on droplet mobility: Ultrahydrophobic surfaces are not always water repellant. *Langmuir* **2006**, *22*, 2433–2436. [CrossRef]
64. Dorrer, C.; Rühe, J. Some thoughts on superhydrophobic wetting. *Soft Matter* **2009**, *5*, 51–61. [CrossRef]
65. Lambley, H.; Schutzius, T.M.; Poulikakos, D. Superhydrophobic surfaces for extreme environmental conditions. *Proc. Natl. Acad. Sci. USA* **2020**, *117*, 27188–27194. [CrossRef]
66. Sojoudi, H.; Kim, S.; Zhao, H.; Annavarapu, R.K.; Mariappan, D.; Hart, A.J.; McKinley, G.H.; Gleason, K.K. Stable wettability control of nanoporous microstructures by iCVD coating of carbon nanotubes. *ACS Appl. Mater. Interfaces* **2017**, *9*, 43287–43299. [CrossRef]
67. Boinovich, L.; Emelyanenko, A.M.; Korolev, V.V.; Pashinin, A.S. Effect of wettability on sessile drop freezing: When superhydrophobicity stimulates an extreme freezing delay. *Langmuir* **2014**, *30*, 1659–1668. [CrossRef]